OPEN

NPG Asia Materials (2017) 9, e344; doi:10.1038/am.2016.205
www.nature.com/am

ORIGINAL ARTICLE

Core-shell and co-doped nanoscale metal-organic particles (NMOPs) obtained via post-synthesis cation exchange for multimodal imaging and synergistic thermo-radiotherapy

Yu Yang[1], Yu Chao[2], Jingjing Liu[2], Ziliang Dong[2], Weiwei He[3], Rui Zhang[2], Kai Yang[3], Meiwan Chen[1] and Zhuang Liu[2]

Nanoscale metal-organic particles (NMOPs) have recently shown great promise in the area of nanomedicine owing to their tunable compositions, highly enriched functionalities, well-defined sizes/shapes and intrinsic biodegradability. Herein, we describe the fabrication of NMOPs with both core-shell and co-doped structures via a post-synthesis cation exchange method for applications in multimodal imaging and combined photothermal and radiation therapy of cancer. Template NMOPs containing Mn^{2+} and IR825, a near-infrared (NIR) dye, are first synthesized and then mixed with Hf^{4+} to obtain core-shell and co-doped Mn/Hf-IR825 NMOPs depending on the dose of added Hf^{4+} ions. In these NMOPs, Mn^{2+} offers strong T1 magnetic resonance (MR) contrast, Hf^{4+} is a high-Z element with excellent computed tomography signal enhancement ability and radio-sensitization capability, and IR825 exhibits rather high NIR absorbance. After coating with polydopamine (PDA) and further conjugation with polyethylene glycol (PEG), the co-doped Mn/Hf-IR825@PDA-PEG particles (NMOP-PEG) showed efficient tumor-homing ability after intravenous injection, as illustrated by MR and photoacoustic (PA) imaging. Utilizing NMOP-PEG achieved excellent tumor killing efficacy through *in vivo* photothermal and radiation synergistic therapy in our mouse tumor model experiments. Importantly, our NMOP-PEG showed no appreciable toxicity to the treated mice and could be efficiently excreted. Our work presents a facile method to fabricate NMOP-PEG with multi-component structures as a biodegradable, multifunctional nanoplatform for multimodal image-guided combination cancer therapy.
NPG Asia Materials (2017) **9,** e344; doi:10.1038/am.2016.205; published online 20 January 2017

INTRODUCTION

Radiation therapy (RT), which is one of the clinically used cancer treatment strategies, in addition to chemotherapy and surgery, utilizes ionizing radiation (X-ray or γ-ray radiation) to ablate tumors without depth restriction.[1–3] However, during RT, only a small fraction of radiation energy is absorbed by tumor cells, whereas normal tissues within the path of the radiation beam are affected in a non-selective manner. Moreover, RT exhibits a relatively low killing efficiency for hypoxic tumor cells owing to the lack of oxygen that is critical for promoting DNA damage by radiation-induced free radicals.[4–7] To enhance the efficacy of RT, tumor-homing nanoagents containing high-Z elements (for example, Au, Hf, Bi and rare earth elements) can effectively concentrate the energy of incident ionizing radiation within the tumor, generating secondary charged particles to improve the RT-induced cancer killing.[8–12] Moreover, in a number of recent studies, photothermal therapy (PTT) with near-infrared (NIR) absorbing agents in local hyperthermia treatment has been found to be able to enhance intratumoral blood flow and increase the oxygenation status in the tumor microenvironment, showing encouraging results for overcoming hypoxia-associated RT resistance.[8,13,14] However, inorganic nanomaterials (for example, Bi_2Se_3,[8] WS_2,[15] CuS@UCNP[11]) with non-biodegradability were used in those studies and their potential for future clinical translation remains unclear.

Metal-organic frameworks or metal-organic particles, which are a class of porous materials consisting of coordination bonds between multidentate organic linkers and metal cations, have shown promise for a wide range of applications.[16–25] In the field of biomedicine, with non-covalent associations between metal ions and organic ligands,

[1]State Key Laboratory of Quality Research in Chinese Medicine, Institute of Chinese Medical Sciences, University of Macau, Avenida da Universidade, Macau, China; [2]Institute of Functional Nano & Soft Materials Laboratory (FUNSOM), Soochow University, Jiangsu, China and [3]School of Radiation Medicine and Protection & School for Radiological and Interdisciplinary Sciences (RAD-X), Jiangsu Provincial Key Laboratory of Radiation Medicine and Protection, Soochow University, Jiangsu, China
Correspondence: Professor M Chen, State Key Laboratory of Quality Research in Chinese Medicine, Institute of Chinese Medical Sciences, University of Macau, Avenida da Universidade, Taipa, Macau 999078, China.
E-mail: mwchen@umac.mo
or Professor Z Liu, Institute of Functional Nano & Soft Materials Laboratory (FUNSOM), Soochow University, 199 Ren-ai Road, Suzhou Industrial Park, Suzhou, Jiangsu 215123, China.
E-mail: zliu@suda.edu.cn
Received 29 May 2016; revised 23 September 2016; accepted 23 October 2016

nanoscale metal-organic particles (NMOPs) possess superior characteristics over many other traditional delivery systems, such as readily modifiable surfaces, well-defined sizes/shapes and intrinsic biodegradability.[26,27] Owing to their tunable compositions, NMOPs have been extensively explored as multifunctional delivery systems for carrying imaging agents, gene therapeutics, chemotherapeutics and photosensitizers, showing promise as an interesting class of theranostic nanoplatforms.[28–36] Recently, based on Mn^{2+} and a NIR dye, IR825, we fabricated Mn-IR825 NMOPs, which showed efficient tumor-homing behavior together with rapid renal excretion for the magnetic resonance (MR) imaging-guided PTT ablation of tumors.[37]

Herein, starting from our previously reported Mn-IR825 NMOPs as nanotemplates, we fabricated both core-shell and co-doped Mn/Hf-IR825 NMOPs via a post-synthesis cation exchange method and then exploited these NMOPs as radiosensitizers and photothermal agents for the combination of PTT and RT. In this nanostructure, Mn^{2+} ions are used as a contrast agent for T1-weighted MR imaging; IR825, with strong NIR absorption, is used as an excellent contrast agent for photoacoustic (PA) imaging and a photothermal agent for PTT; and Hf^{4+}, with a high-Z number, not only offers contrast for X-ray computed tomography (CT) imaging but also endows NMOPs with strong X-ray absorbance for enhanced RT. The NMOPs are then coated with polydopamine (PDA) and further modified with polyethylene glycol (PEG) to confer excellent physiological stability. As indicated by triple-modal MR/PA/CT imaging, these Mn/Hf-IR825 Mn/Hf-IR825@PDA-PEG particles (NMOP-PEG) nanoparticles show efficient tumor retention. The *in vivo* combination of PTT and RT was thus performed in a mouse tumor model with intravenous injection of co-doped NMOP-PEG. The two therapies demonstrate a strong synergistic treatment effect that is attributed to the significantly increased oxygenation induced by the mild hyperthermia of PTT to improve the blood flow into the tumor as well as the capability of Hf to sensitize RT. Importantly, owing to the biodegradability of Mn/Hf-IR825 NMOPs, we observed almost complete excretion of Hf from the mouse body and no obvious long-term toxicity from NMOP-PEG in the treated mice within a month. Our work presents a facile post-synthesis cation exchange method to synthesize core-shell and co-doped NMOPs that can act as biodegradable and versatile nanoplatforms with highly integrated biomedical imaging and therapy functions.

MATERIALS AND METHODS

Materials

Manganese chloride ($MnCl_2$) and hafnium chloride ($HfCl_4$) were obtained from Alfa Aesar (China) Chemical Co. Ltd. Dopamine and poly(maleic anhydride-alt-1-octadecene) (C_{18}PMH) were purchased from Sigma-Aldrich (Shanghai, China). Polylactide-poly(ethylene glycol) (PEG-NH_2, MW = 5 K) was purchased from Biomatrik Inc (Jiaxing, China). Other chemicals were obtained from Sinopharm Group Co. Ltd (Shanghai, China). All chemicals were used as received without further purification.

Synthesis of Mn-IR825 NMOPs

Mn-IR825 NMOPs were prepared according to the previous literature.[38] In a typical synthesis experiment, 4 mg of IR825 dissolved in a methanol-triethylamine (50:1) mixture was added into 20 ml of a methanol/*N*,*N*-dimethylformamide (DMF) (V/V: 85/15) solution of manganese chloride. The mixture was ultrasonicated for 6 h and stirred for another 12 h at 30 °C. Subsequently, 10 mg of poly(vinyl pyrrolidone) (MW = 30 K) as a dispersing and stabilizing agent was added and stirred for another 60 h to obtain the Mn-IR825 nanoscale coordination polymer nanoparticles (NMOPs).

Synthesis of Hf-IR825 NMOPs

Three milligrams of IR825 and 9 mg of $HfCl_4$ were dissolved in 20 ml of a methanol/DMF (V/V: 85/15) solution. Next, 200 μl of triethanolamine was added to the mixture. After ultrasonication for another 2 h, the Hf-IR825 NMOPs were obtained.

Synthesis of Mn/Hf-IR825 NMOPs

The as-prepared Mn-IR825 NMOPs dispersed in 20 ml of methanol/DMF (V/V: 85/15) were added to 10 μl of $HfCl_4$ (10 mg ml^{-1}) and reacted for 10 min at room temperature to obtain core-shell Mn/Hf-IR825 NMOPs. To prepare co-doped Mn/Hf-IR825 NMOPs, 200 μl of $HfCl_4$ (10 mg ml^{-1}) was added into the above sample, which was then ultrasonicated for 2 h. After another 24 h of stirring, the resulting co-doped NMOPs were washed with methanol three times to remove excess unreacted reagents.

Synthesis of Mn/Hf-IR825@PDA-PEG

The Mn/Hf-IR825 solution was stirred for 30 min before 2 mg of dopamine was added into the mixture at pH 8.5. After further stirring for 12 h, the resulting Mn/Hf-IR825@PDA nanoparticles were concentrated by rotary evaporation and washed with deionized water three times. Next, another 200 mg of C_{18}PMH-PEG was added into the obtained Mn-IR825@PDA sample, which was then stirred overnight. After purification by ultrafiltration, the obtained Mn-IR825@PDA-PEG particles were stored at 4 °C for further use.

Cellular culture experiments

Murine breast cancer 4T1 cells, human embryonic kidney 293T cells and human epithelial carcinoma HeLa cells were purchased from the American Type Culture Collection and cultured in standard cell culture medium containing 10% fetal bovine serum and 1% penicillin/streptomycin at 37 °C in a 5% CO_2-containing atmosphere. For the *in vitro* cytotoxicity assay, 4T1, A549 and HeLa cells were seeded onto 96-well plates at a density of 1×10^5 per well for 24 h of incubation and then treated with different concentrations of the Mn/Hf-IR825@PDA-PEG particles (NMOP-PEG) for 24 h. Finally, the relative cell viabilities were measured by standard 3-(4,5-dimethylthiazol-2-yl)-2,5-diphenyltetrazolium bromide assays. For *in vitro* PTT, 4T1 cells were seeded onto 96-well plates at a density of 1×10^5 per well for 24 h and then treated with various concentrations of NMOP-PEG. After incubation for 2 h, the cells were irradiated by an 808-nm NIR laser at a density of 0.3 W cm^{-2} for 15 min. The standard methyl thiazolyl tetrazolium assay was used for determining the relative cell viabilities. For confocal imaging, the cells were stained with calcein AM/propidium iodide and imaged by a Leica SP5 laser scanning confocal microscope.

For the clonogenic assay, 4T1 cancer cells were seeded onto six-well plates at densities of 100, 200, 500, 1000 and 2000 per well and incubated at 37 °C for 24 h. Then, cells were treated with 30 μg ml^{-1} NMOP-PEG for 6 h, while cells without treatment with NMOP-PEG were used as the control. Next, the cells were exposed to X-ray irradiation at various radiation doses (0, 2, 4, 6 and 8 Gy). After being washed with PBS and further incubated for 10 days at 37 °C, the cells were fixed with anhydrous ethanol and stained with crystal violet (Sigma-Aldrich). The resulting cell colonies were only calculated if they contained >50 cells. The surviving fraction was calculated as follows: (surviving colonies)/(cells seeded × plating efficiency) × 100%. The mean surviving fraction was obtained from three parallel tests.

For the γ-H2AX immunofluorescence analysis, 4T1 cancer cells seeded on 12-well plates were incubated with 0 or 30 μg ml^{-1} NMOP-PEGs for 6 h and then irradiated with X-ray irradiation at a dose of 6 Gy. After 2 h of incubation, the cells were fixed by 4% of paraformaldehyde for 10 min and then washed with PBS three times. Then, the cells were permeabilizated with methanol for 15 min at −20 °C and washed with PBS. Afterwards, the cells were exposed to blocking buffer (1% BSA in PBS solution) for 1 h at room temperature and further incubated with the primary antibody (anti-phospho-histone γ-H2AX mouse monoclonal antibody, dilution of 1:500) for 12 h at 4 °C. After washing with PBS, the cells were incubated with the secondary antibody (Cy3-conjugated sheep anti-mouse secondary antibody, dilution of 1:500) for 1 h at 37 °C. Excess antibody was washed by rinsing the coverslips in PBS. Cell nuclei were stained with 2-(4-amidinophenyl)-6-indolecarbamidine

dihydrochloride for 5 min at room temperature. The cells were imaged using confocal microscopy (Leica SP5).

In vivo tumor model

Balb/c mice were purchased from Nanjing Pengsheng Biological Technology Co. Ltd (Nanjing, China). and used according to the protocols approved by the Soochow University Laboratory Animal Center. To develop the tumor model, 4T1 cells (2×10^6) suspended in 25 μl of serum-free Rosewell Park Memrial Institute-1640 medium were subcutaneously injected into the back of each Balb/c mouse.

Multimodal imaging

For MR imaging, NMOP-PEG at concentrations ranging from 0 to 1 mM (in terms of Mn) were scanned under a 3T clinical MRI scanner at room temperature. The T1-weighted MR signal intensity of each sample was acquired from MR images in the region of interest. The relaxation rate R1 was then calculated from T1 at various Mn^{2+} concentrations. For *in vivo* MR imaging, Balb/c mice bearing 4T1 tumors were scanned with the same 3T clinical MRI scanner, equipped with a special animal imaging coil, before and after intravenous injection with NMOP-PEG (5 mg kg^{-1} for each mouse).

For CT imaging, NMOP-PEG at various concentrations ranging from 0 to 50 mg kg^{-1} were scanned by a GE discovery CT750 HD scanner (GE Healthcare, WI, USA) (beam collimation = 64 × 0.625 mm; table speed = 27 mm per rotation; beam pitch = 1.25; gantry rotation time = 1.0 s.). For *in vivo* imaging, tumor-bearing mice were intravenous injected with NMOP-PEG (30 mg kg^{-1}). CT images were obtained before and 24 h after injection of NMOP-PEG.

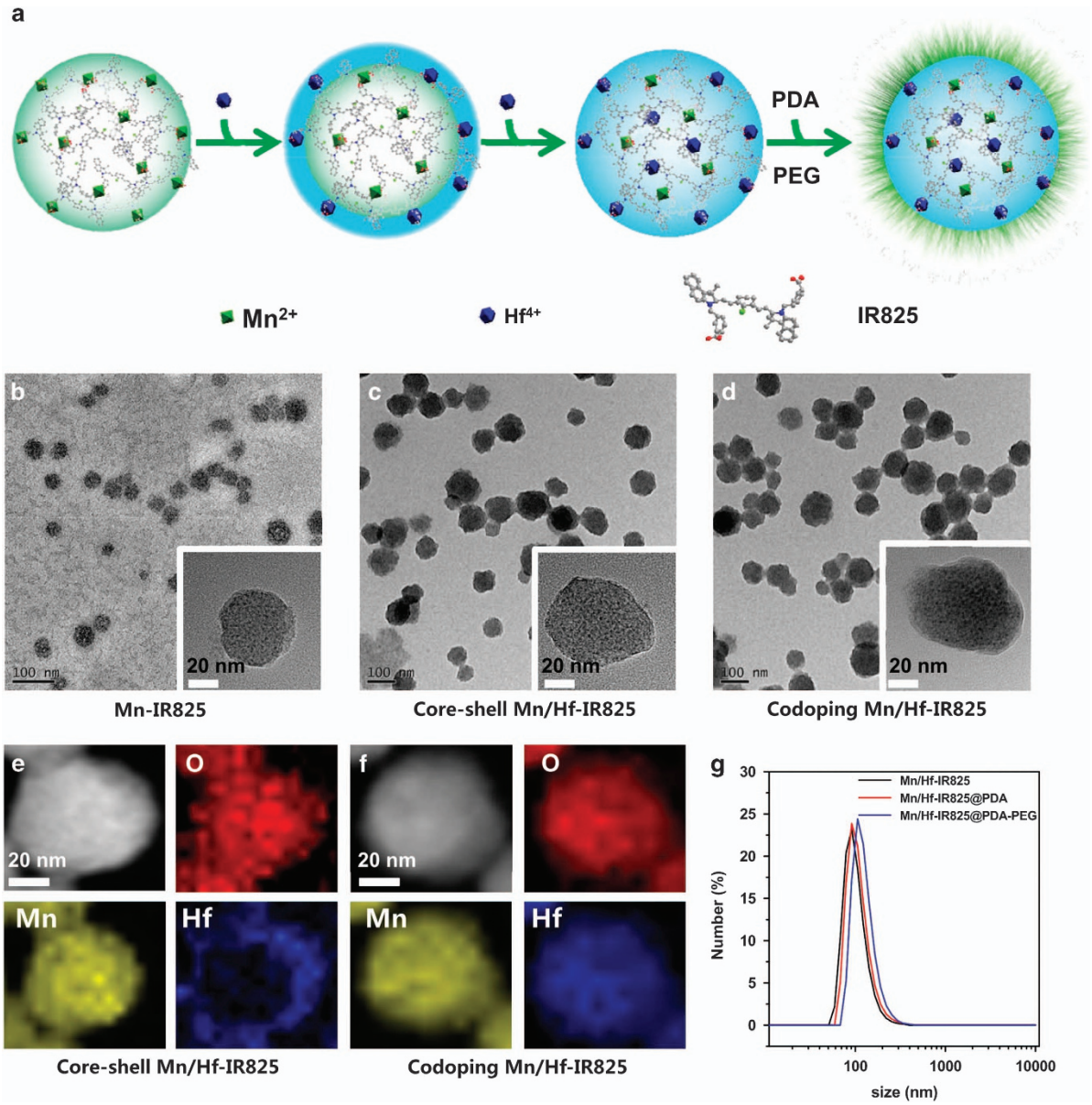

Figure 1 Synthesis and characterization of Mn/Hf-IR825 NMOPs. (**a**) A schematic illustration showing the fabrication of core-shell and co-doped Mn/Hf-IR825 NMOPs via the post-synthesis cation exchange method and the subsequent surface coating with PDA and PEG. (**b**–**d**) TEM images of the as-synthesized Mn-IR825 (**b**), core-shell Mn/Hf-IR825 (**c**) and co-doped Mn/Hf-IR825 (**d**) NMOPs. Insets are the respective higher resolution TEM images. (**e**, **f**) HAADF-STEM images of core-shell (**e**) and co-doped (**f**) Mn/Hf-IR825 NMOPs. The element maps show the distribution of O (red), Mn (yellow) and Hf (blue). (**g**) The hydrodynamic diameters of co-doped Mn/Hf-IR825, Mn/Hf-IR825@PDA and Mn/Hf-IR825@PDA-PEG nanoparticles (NMOP-PEG).

For PA imaging, mice were intravenous injected with NMOP-PEG when the tumor reached ~ 70 cm^3. Mice were anaesthetized, and their tumors were scanned using the VisualSonics Vevo 2100 LAZR system (LZ400 probe, 30 MHz, 256-element linear array transducer).

In vivo PTT& RT combined therapy

Balb/c mice bearing 4T1 tumors were randomly divided into seven groups after their tumors had reached ~ 60 cm^3 ($n = 5$ for each group): (a) control, (b) intravenous injection of NMOP-PEG, (c) NIR laser only (808 nm, 0.6 W cm^{-2}, 5 min), (d) NMOP-PEG+NIR laser, (e) RT only, (f) NMOP-PEG+RT and (g) NMOP-PEG+laser+RT. The dose of NMOP-PEG was 20 mg kg^{-1}, in terms of Hf, in the above groups. After 24 h, the tumors of groups (e) and (f) were exposed to X-ray irradiation at a dose of 6 Gy, and the tumors of groups (b) and (e) were irradiated by an 808-nm NIR laser at a power density of 0.4 W cm^{-2} for 20 min. The tumor temperature was recorded by an infrared camera (IRS E50 Pro Thermal Imaging Camera).

After the different treatments, the tumor size was measured by a digital caliper every 2 days and calculated according to the following formula: the volume = (tumor length) × (tumor width)^2/2. The relative tumor volumes were determined as V/V_0 (V_0 is the initial volume). Two days after the various treatments, the tumors were collected to make paraffin sections for further hematoxylin and eosin (H&E) staining according to the manufacturer's protocol.

In vivo biodistribution and toxicity studies

To determine the blood circulation behavior of NMOP-PEG, blood was collected from each mouse at indicated time points, weighed and then dissolved with digestive aqua regia (HCl: HNO_3 = 3:1) to analyze the total amount of Mn in the blood using inductively coupled plasma-atomic emission spectroscopy (ICP-AES).

For the biodistribution and toxicology study, Balb/c mice were intravenous injected with 0.2 ml of 2 mg ml^{-1} NMOPs and killed at different time points (1 day, 7 days, 14 days and 30 days post injection, $n = 5$ mice per group) after injection. Blood samples were collected for blood panel and blood chemistry analysis before the mice were killed; then, the major organs were collected for biodistribution. To determine the biodistribution of our NMOPs, liver, spleen, kidney, heart, lung, stomach, intestine, skin, muscle, bone and tumor samples were harvested at the indicated time points and solubilized by aqua regia for ICP-AES measurement to determine the Hf levels in various organs. For histological examination, the harvested organs (liver, spleen, kidney, heart and lung) were fixed in 10% neutral buffered formalin and then treated by paraffin for H&E staining. The H&E-stained organ slices were observed on a digital microscope (Leica QWin, Buffalo Grove, IL, USA).

RESULTS AND DISCUSSION

NMOPs composed of metal ions and IR825 ligands were fabricated in a mixed solvent of DMF and methanol via the post-synthesis cation exchange method (Figure 1a). First, Mn-IR825 NMOPs were synthesized after addition of IR825 into a solution of manganese chloride dissolved in methanol/DMF (V/V: 85/15) at 30 °C. The as-prepared Mn-IR825 NMOPs exhibited relatively uniform sizes, as observed by transmission electronic microscopy (Figure 1b, Supplementary Figure S2). Furthermore, we extended our method to synthesize Hf-IR825 NMOPs. As revealed by TEM imaging (Supplementary Figure S1), energy-dispersive X-ray spectroscopy elemental mapping (Supplementary Figure S3) and powder X-ray diffraction patterns (Supplementary Figure S3), the Hf-IR825 NMOPs were successfully synthesized, exhibiting amorphous structures with uniform morphology.

To synthesize core-shell NMOPs, a $HfCl_4$ solution was added into the as-prepared Mn-IR825 mixture under ultrasonication. Interestingly, when we changed the amount of injected $HfCl_4$ and the reaction time, the nanostructure of the NMOPs could be tuned. After a small amount of Hf^{4+} was injected and had reacted for 10 min, Mn^{2+} was partially exchanged by Hf^{4+} in the outer layer of the Mn-IR825 NMOPs, resulting in the formation of core-shell

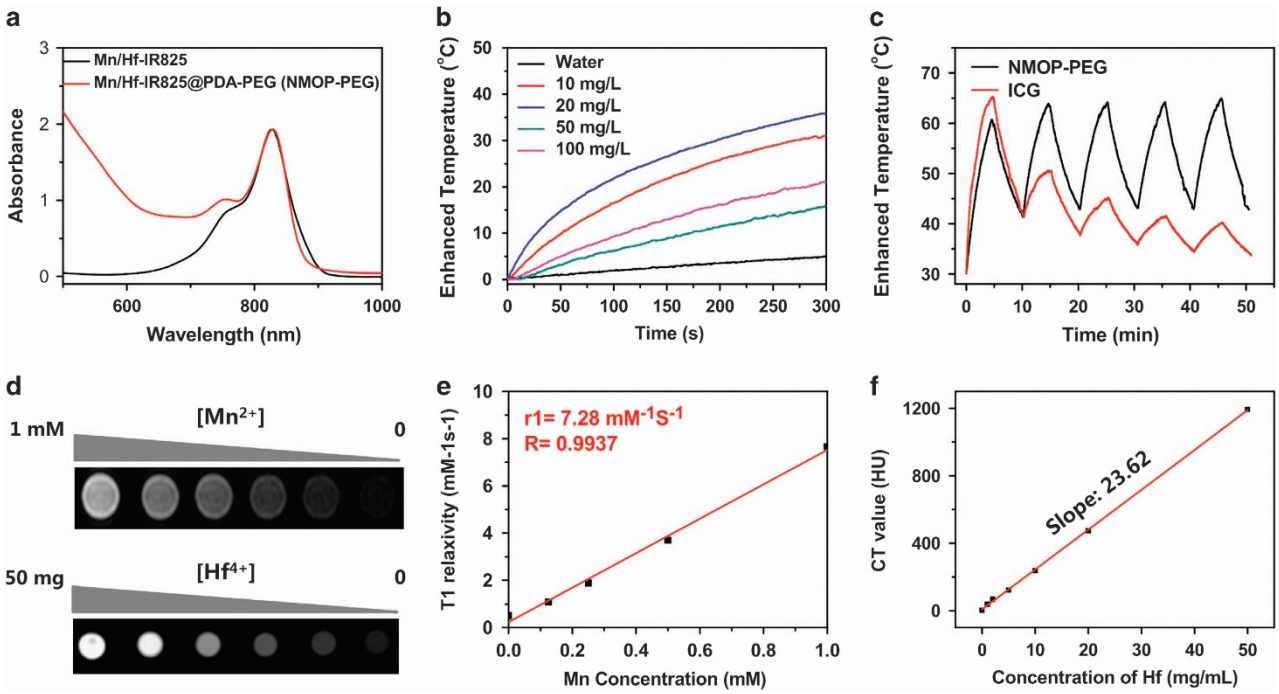

Figure 2 Characterization of co-doped Mn/Hf-IR825@PDA-PEG (NMOP-PEG). (**a**) UV-vis-NIR absorbance spectra of Mn/Hf-IR825 and Mn/Hf-IR825@PDA-PEG. (**b**) The heating curves of a solution of NMOP-PEG at different concentrations upon exposure to 808-nm light at a power density of 0.7 W cm^{-2} for 5 min. (**c**) Temperature curves of NMOP-PEG and ICG solutions under five cycles of laser-induced photothermal heating. (**d**) T1-weighted MR images (the top row) and CT images (the bottom row) of NMOP-PEG at various concentrations. (**e**, **f**) T1 relaxation rates (**e**) and HU values (**f**) of NMOP-PEG at various concentrations.

Mn/Hf-IR825 NMOPs that were detected by energy-dispersive X-ray spectroscopy elemental mapping in TEM (Figures 1c and e). With a further increase in added Hf^{4+}, the structure of the Mn/Hf-IR825 NMOPs gradually changed from a core-shell structure into a co-doped structure (Figures 1d and f). Similar to the Mn-IR825 NMOPs reported in our previous work[37], the Mn/Hf-IR825 NMOPs also exhibited a spherical morphology and amorphous structure after the addition Hf^{4+} ions, indicating that their structure was maintained during the process of creating Mn/Hf-IR825 NMOPs (Supplementary Figure S3). The thermogravimetric-differential thermal analysis of the Mn/Hf-IR825 NMOPs indicated that the mass ratio of IR825 was 57.5%. (Supplementary Figure S4). Meanwhile, it was found that the molar ratio of Mn:Hf increased from 1:0 in the Mn-IR825 NMOPs to 1:0.626 in the co-doped Mn/Hf-IR825 NMOPs prepared by simply adding $HfCl_4$ into the original Mn-IR825 NMOP mixture under sonication for 2 h. Therefore, the formation of Mn/Hf-IR825 NMOPs likely proceeds via the cation exchange process using Mn-IR825 as a template.

To further functionalize the NMOPs, we coated as-synthesized co-doped Mn/Hf-IR825 NMOPs with PDA and PEG-grafted amphiphilic polymers to enhance their water stability and physiological stability. We obtained Mn/Hf-IR825@PDA-PEG nanoparticles (abbreviated as NMOP-PEG in the following parts of this paper) with an average hydrodynamic diameter of ~110 nm (Figure 1g, Supplementary Figure S5). The physical properties of NMOP-PEG were then investigated in detail. As expected, owing to the high NIR absorbance of IR825,[38] both the Mn/Hf-IR825 NMOPs and NMOP-PEG showed a strong NIR absorption peak at 825 nm (Figure 2a). The mass extinction co-efficient of Mn/Hf-IR825 was measured as 74.5 $l\,g^{-1}\,cm^{-1}$ at 808 nm, which was similar to that of our previously reported Mn-IR825 NMOPs (78.2 $l\,g^{-1}\,cm^{-1}$) and much higher than that of many other photothermal agents such as reduced graphene oxide (21.1 $l\,g^{-1}\,cm^{-1}$), MoS_2 nanosheets (28.4 $l\,g^{-1}\,cm^{-1}$), single-walled carbon nanotubes (46.5 $l\,g^{-1}\,cm^{-1}$) and polypyrrole (62 $l\,g^{-1}\,cm^{-1}$). Furthermore, NMOP-PEG showed excellent photothermal conversion efficiency and could be rapidly heated under 808-nm NIR laser irradiation (Figure 2b, Supplementary Figure S6). After five cycles of NIR laser exposures (5 min every cycle, 0.6 W cm^{-2}), NMOP-PEG showed high photostability, whereas ICG, an Food and Drug Administration approved NIR dye, showed obvious decay in its NIR absorption (Figure 2c).

Mn^{2+} with low bio-toxicity has been considered as a great T1 MR contrast agent owing to its five unpaired 3d electrons.[39–41] T1-weighted MR images of various concentrations of NMOP-PEG acquired by a 3T MR scanner showed a concentration-dependent brightening effect (Figure 2d). The corresponding longitudinal relaxivity (r1) value of the NMOP-PEG was measured to be 7.28 $ms^{-1}\,S^{-1}$, which is higher than that of Magnevist, a commercially used Gd-based contrast agent (4.25 $ms^{-1}\,S^{-1}$),[42] justifying the use of NMOP-PEG as a T1-weighted MR contrast agent (Figure 2e). In the meanwhile, owing to the high X-ray absorption co-efficient of Hf,[43] the NMOP-PEG generated strong contrast under CT imaging,

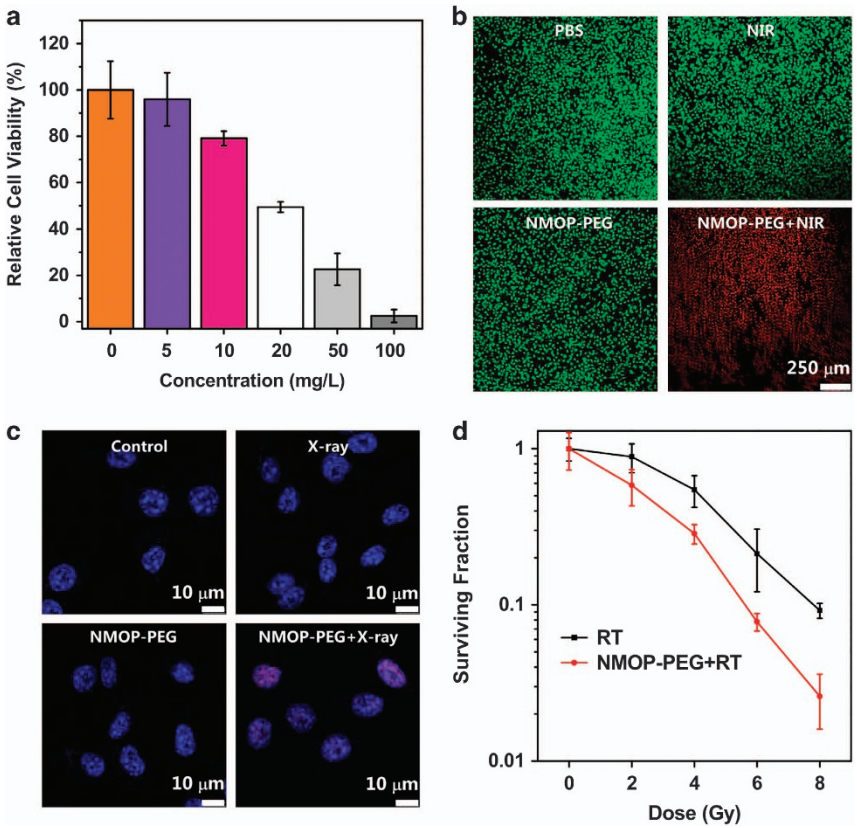

Figure 3 *In vitro* photothermal therapy and enhanced radiation therapy. (**a**) Relative viabilities of 4T1 cells incubated with different concentrations of NMOP-PEG after 808-nm laser irradiation at a density of 0.5 W cm^{-2} for 5 min. (**b**) Confocal images of calcein AM and propidium iodide co-stained 4T1 cells treated with PBS, NIR, NMOP-PEG and NMOP-PEG+NIR (0.1 mg ml^{-1}, 0.5 W cm^{-2}, 10 min). (**c**) Confocal images of γ-H2AX-stained cells treated with PBS, RT (6 Gy), NMOP-PEG and NMOP-PEG+RT (6 Gy). The 4T1 cells treated with NMOP-PEG+RT showed the highest DNA damage. (**d**) Clonogenic survival assay of 4T1 cells treated with and without NMOP-PEG under various X-ray radiation doses.

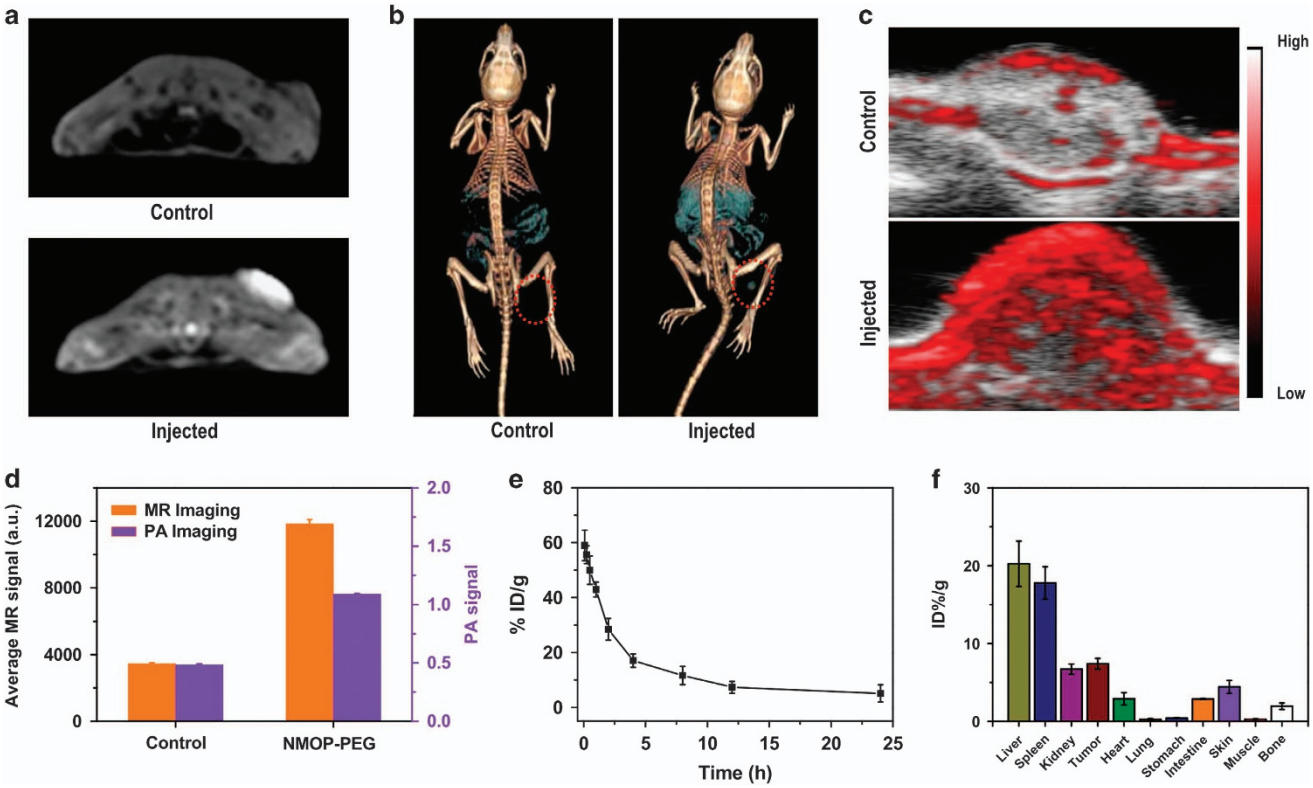

Figure 4 *In vivo* imaging with NMOP-PEG. (**a**–**c**) *In vivo* T1-weighted MR images (**a**), CT images (**b**) and PA images (**c**) of tumor-bearing mice before and 24 h after i.v. injection with NMOP-PEG. PA imaging was conducted on the tumor region. (**d**) Quantified MR and PA signals of tumors from mice before (control) and 24 h after i.v. injection of NMOP-PEG. (**e**) Time-dependent blood circulation of NMOP-PEG. (**f**) Biodistribution of NMOP-PEG in 4T1 tumor-bearing mice at 24 h p.i. NMOP-PEG levels in (**e** and **f**) are based on the ICP-AES-measured Hf levels in the blood and various organs.

showing an obvious concentration-dependent enhancement effect (Figure 2d). As shown in Figure 2f, the slope in Hounsfield units (HU) of NMOP-PEG was measured to be 23.62 HU l g^{-1}, which is much higher than the commercially used iodine-based CT contrast agent, iopromide (15.9 HU l g^{-1}).[44]

Next, we studied the *in vitro* cytotoxicity of our NMOP-PEG material as well as its capability as a photothermal and radio-sensitizing agent at the cellular level. With a biocompatible PDA and PEG coating, the NMOP-PEG did not show an appreciable toxic effect to 4T1 cells (a murine breast cancer cell line), KB cells (human carcinoma cells) and 293T cells (a human embryonic kidney cell line) after incubation for 24 h even with a high concentration up to 100 mg l^{-1}, as evaluated by the methyl thiazolyl tetrazolium and LDH leakage assays (Supplementary Figures S7 and S8). Considering the strong NIR absorbance of NMOP-PEG, various concentrations of NMOP-PEG were added to 4T1 cancer cells for *in vitro* PTT under irradiation by an 808-nm NIR laser at a density of 0.6 W cm^{-2}. The cell viability assay indicated enhanced ablation of 4T1 cells with increasing concentrations of NMOP-PEG after NIR-induced PTT (Figure 3a), whose efficacy at killing cancer cells was also vividly illustrated by confocal imaging of calcein AM and propidium iodide double-stained 4T1 cells after different treatments (Figure 3b).

Owing to the intense X-ray attenuation ability of the Hf in NMOP-PEG,[45,46] the radio-sensitization of NMOP-PEG nanoparticles was also evaluated *in vitro* using X-rays to trigger RT. Samples of 4T1 cells were cultured in the absence or presence of NMOP-PEG (10 μg ml^{-1}) for 24 h and then exposed to X-rays at various doses. The clonogenic assay was conducted 10 days after the X-ray exposure of the cells (Figure 3d). It was found that incubation with NMOP-PEG could remarkably reduce the percentages of viable cell colonies after different doses of RT treatment, evidencing the strong radio-sensitizing effect of NMOP-PEG. To evaluate the DNA damage in 4T1 cells caused by RT, anti-γ-H2AX, a DNA damage marker was introduced for immunofluorescent cell staining (Figure 3c). Although no detectable or weak γ-H2AX fluorescence was observed in the cells incubated with NMOP-PEG without X-ray irradiation and those exposed to X-rays (6 Gy) in the absence of NMOP-PEG, obvious γ-H2AX fluorescence spots were observed in the nuclei of cells irradiated by X-rays (6 Gy) after treatment with NMOP-PEG, demonstrating the capability of NMOP-PEG to enhance RT-induced DNA damage of cancer cells. Therefore, this radio-sensitizing effect may be attributed to the photoelectric effect and Compton scattering of Hf-containing NMOP-PEG nanoparticles to absorb and concentrate the radiation dose inside cells, increase the radiation-induced DNA damage and then inhibit the proliferation of cancer cells.[47]

Subsequently, the capability of NMOP-PEG to act as a multimodal imaging agent was utilized to study the *in vivo* behaviors of the nanoparticles. After intravenous injection of NMOP-PEG (10 mg kg^{-1}), mice bearing 4T1 tumors were imaged by a 3T clinical MR scanner equipped with a small animal imaging coil. Remarkable T1-weighted MR signals showed up in the tumor at 24 h post injection with NMOP-PEG, indicating the significant accumulation of NMOP-PEG in the tumor via the enhanced permeability and retention effect (Figure 4a). For quantitative analysis, the average MR signal in the tumor at 24 h post intravenous injection of the NMOP-PEG increased to ~ 344% compared with that before NMOP-

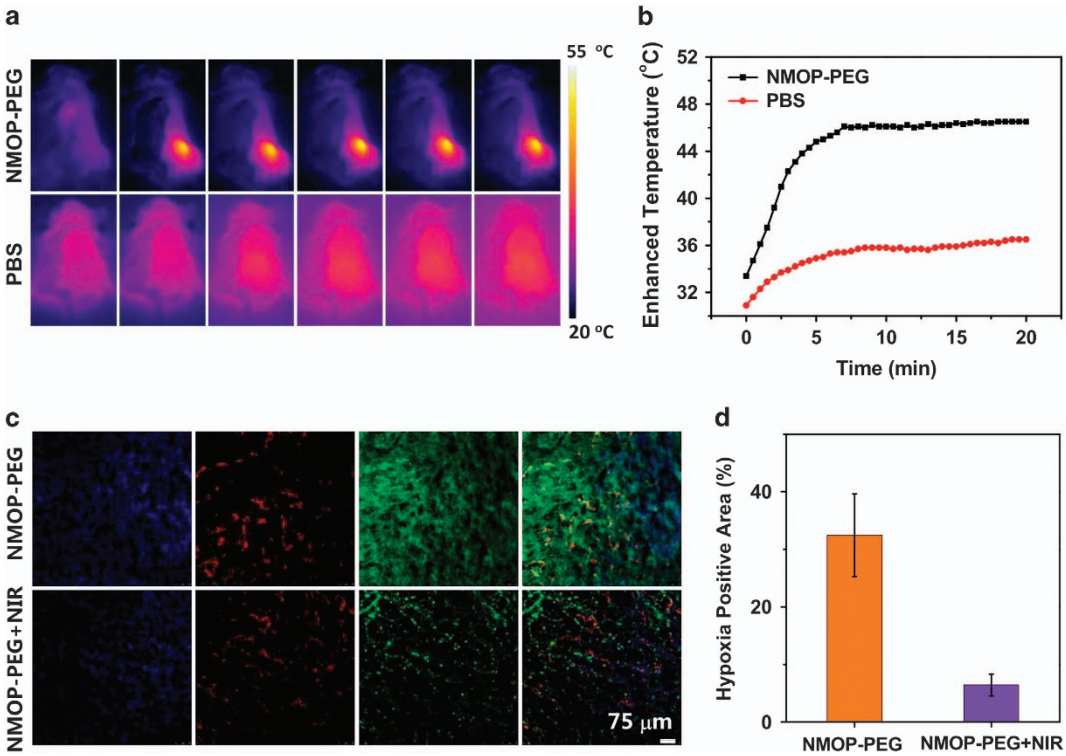

Figure 5 *In vivo* photothermal heating with NMOP-PEG. (**a**) IR thermal images of tumor-bearing mice with i.v. injection of NMOP-PEG (upper row, dose = 20 mg kg^{-1}) or PBS irradiated by an 808-nm laser at a density of 0.3 W cm^{-2} for 20 min. (**b**) Temperature changes of tumors recorded by an IR thermal camera under NIR laser irradiation in **a**. (**c**, **d**) Immunofluorescence images (**c**) and the quantified relative hypoxia-positive areas (**d**) of tumor slices from mice injected with NMOP-PEG with or without NIR laser irradiation (808 nm, 0.3 W cm^{-2} for 20 min). The cell nuclei, blood vessels and hypoxia areas were stained by DAPI (blue), anti-CD31 antibody (red) and anti-pimonidazole antibody (green), respectively.

PEG injection (Figure 4d). Next, *in vivo* CT imaging was performed by injecting 4T1 tumor-bearing mice with NMOP-PEG (30 mg kg^{-1}). As shown in Figure 4b, strong CT contrast showed up in the tumor at 24 h post injection of NMOP-PEG, indicating efficient nanoparticle uptake by the tumor. In addition, the liver contrast was also increased after injection with NMOP-PEG, suggesting nanoparticle retention in the liver, which belongs to the reticuloendothelial system that is responsible for the clearance of foreign nanoparticles from blood circulation.

PA imaging, which is based on the generation of acoustic waves induced by the tissue absorbance of light, offers significantly increased spatial resolution and imaging depth in comparison with traditional *in vivo* optical imaging.[48–52] NMOP-PEG with strong NIR absorbance could be an effective contrast agent for PA imaging. After intravenous injection of NMOP-PEG, mice bearing 4T1 tumors were imaged under a PA imaging system with an 860-nm laser as the excitation source. Owing to the passive tumor accumulation of NMOP-PEG, the PA signals in the tumor region significantly increased at 24 h post injection, whereas the initial PA signals in the tumor without injection of NMOP-PEG were quite weak (Figure 4c). Consistent with the MR imaging and CT imaging results, significantly enhanced PA signals in the whole tumor indicated that a large amount of NMOP-PEG nanoparticles had homogenously accumulated inside the tumor after systemic administration.

For a more accurate understanding of the *in vivo* behavior of NMOP-PEG, we quantitatively measured Hf^{4+} levels in the blood and different organs using ICP-AES (Figures 4e and f). After injection of NMOP-PEG, a gradual decay of the blood levels of NMOP-PEG was observed over time. The pharmacokinetics of NMOP-PEG followed a two-compartment model, with the first and second phases of the blood circulation half-lives determined as 1.09 ± 0.47 h and 12.7 ± 3.06 h, respectively. The long blood half-lives of the nanoparticles are favorable for their passive tumor accumulation via the enhanced permeability and retention effect. Consistent with the CT, MR and PA imaging results, NMOP-PEG exhibited a relatively high tumor accumulation of ~7.4% of injected dose per gram tissue (%ID g^{-1}) at 24 h post injection of NMOP-PEG.

Motivated by the capability of the NMOP-PEG nanoparticles to trigger PTT and enhanced RT *in vitro* as well as their efficient tumor accumulation mediated by the enhanced permeability and retention effect, the *in vivo* synergistic therapeutic effect of PTT and RT induced by NMOP-PEG was then evaluated in 4T1 tumor-bearing mice. After being intravenous injected with 200 μl of NMOP-PEG (2 mg ml^{-1}) for 24 h, mice bearing 4T1 tumors were irradiated with an 808-nm NIR laser at a power density of 0.3 W cm^{-2}. An infrared thermal camera was utilized to monitor the temperature change on the surface of the tumor during laser irradiation. After NIR irradiation for 20 min, the tumor temperature for mice intravenous injected with 20 mg kg^{-1} NMOP-PEG increased from 33.3 to ~46 °C, whereas that for PBS injected mice showed a much less-significant increase under the same irradiation conditions (only ~36 °C post laser irradiation) (Figures 5a and b).

In previous studies, it has been found that moderate PTT or other local hyperthermia treatments could improve the tumor oxygenation status by promoting intratumoral blood flow.[53,54] To evaluate the effect of PTT on tumor hypoxia in our experiments, an immunofluorescence staining assay was performed by staining the hypoxic areas, blood vessels and cell nuclei with anti-pimonidazole antibody,

anti-CD31 antibody and 2-(4-amidinophenyl)-6-indolecarbamidine dihydrochloride, respectively (Figure 5c). The pimonidazole-stained (green) hypoxic area in the tumor treated with NMOP-PEG+NIR was significantly weaker than that in the control without NIR irradiation. Quantitative analysis of the hypoxia-positive areas further demonstrated the effective improvement of tumor oxygenation after mild photothermal treatment with NMOP-PEG (Figure 5d). Next, we evaluated the *in vivo* cancer treatment efficacy of the combination of PTT and RT with NMOP-PEG using Balb/c mice bearing 4T1 tumors. In our therapy experiments, 4T1 tumor-bearing mice were divided into seven groups: (a) PBS, (b) PBS+NIR, (c) intravenous injected NMOP-PEG, (d) intravenous injected NMOP-PEG+NIR, (e) X-ray irradiation (RT only), (f) intravenous injected with NMOP-PEG+RT and (g) intravenous injected with NMOP-PEG+NIR+RT. The dose of NMOP-PEG was 20 mg kg^{-1} in the above groups. NIR light irradiation was applied at a power density of 0.3 W cm^{-2} for 20 min, whereas the X-ray radiation dose for RT was 6 Gy. The tumor sizes were measured after the above treatments were conducted (Figure 6a). At day 14 post treatment, tumors from the various groups were collected and weighed (Figure 6b, Supplementary Figure S10). As expected, NMOP-PEG injection alone or NIR irradiation alone (without NMOP-PEG) had no effect on the tumor growth. The moderate PTT treatment after intravenous injection of NMOP-PEG exposed to the low power NIR laser exhibited partial inhibitory effects on the tumor growth. Meanwhile, compared with RT only (group d), the efficacy of RT showed a certain degree of enhancement after injection of NMOP-PEG owing to the radio-sensitization effect of the Hf^{4+}-containing nanoparticles. However, the tumor growth rate in all the above groups still increased at later time points. Interestingly, we found that treatment with NMOP-PEG+NIR+RT showed an excellent tumor growth inhibition effect, with the majority of tumors (four out of five) in this group completely eliminated without recurrence during 14 days, demonstrating the remarkable synergistic effect of the combined PTT and RT with NMOP-PEG in comparison with the respective mono-therapies. Moreover, H&E staining was conducted on tumors from various groups 2 days after the different treatments had been completed (Figure 6c). After combination therapy by NMOP-PEG+NIR+RT treatment, the tumor cells were severely destructed, as indicated by the condensed nuclei, additional vacuoles and changed cell shapes found in this group, whereas the structures of the tumor cells in other control groups were either not affected or partially destroyed.

Therefore, our results collectively demonstrate that the combination of PTT and RT using Mn/Hf-IR825 NMOP-PEG nanoparticles induces an excellent synergistic effect for cancer treatment. This synergistic therapeutic effect was attributed to the following facts. On the one hand, the photoelectric and Compton scattering effect of Hf-containing NMOP-PEG concentrated the radiation dose inside the tumor to accelerate X-ray-induced DNA breakage. On the other hand, the presence of a hypoxic region in the tumor microenvironment was greatly relieved after mild PTT treatment, which is known to promote intratumoral blood flow.[8,54] Therefore, the mild PPT enhanced the overall tumor oxygenation status and then decreased the hypoxia-

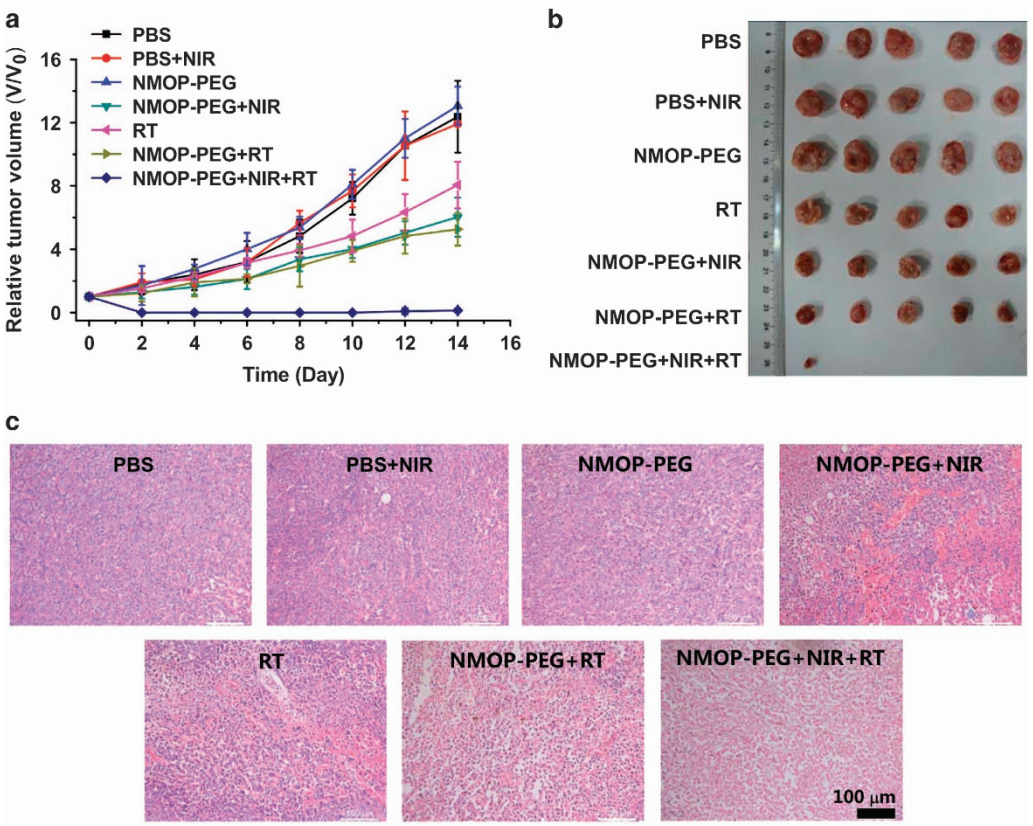

Figure 6 *In vivo* synergistic thermo-radiotherapy. (**a**) The tumor volume growth curves of mice after different treatments: (i) PBS, (ii) PBS+NIR, (iii) NMOP-PEG, (iv) NMOP-PEG+NIR, (v) RT, (vi) NMOP-PEG+RT, (vii) NMOP-PEG+NIR+RT. NIR laser irradiation was conducted using an 808-nm with a density of 0.3 W cm^{-2} for 20 min. The X-ray radiation dose was 6 Gy for RT. (**b**) A photograph of tumors collected from mice that had undergone various treatments at day 14. (**c**) H&E-stained tumor slices collected from various groups of mice at 2 days post treatment.

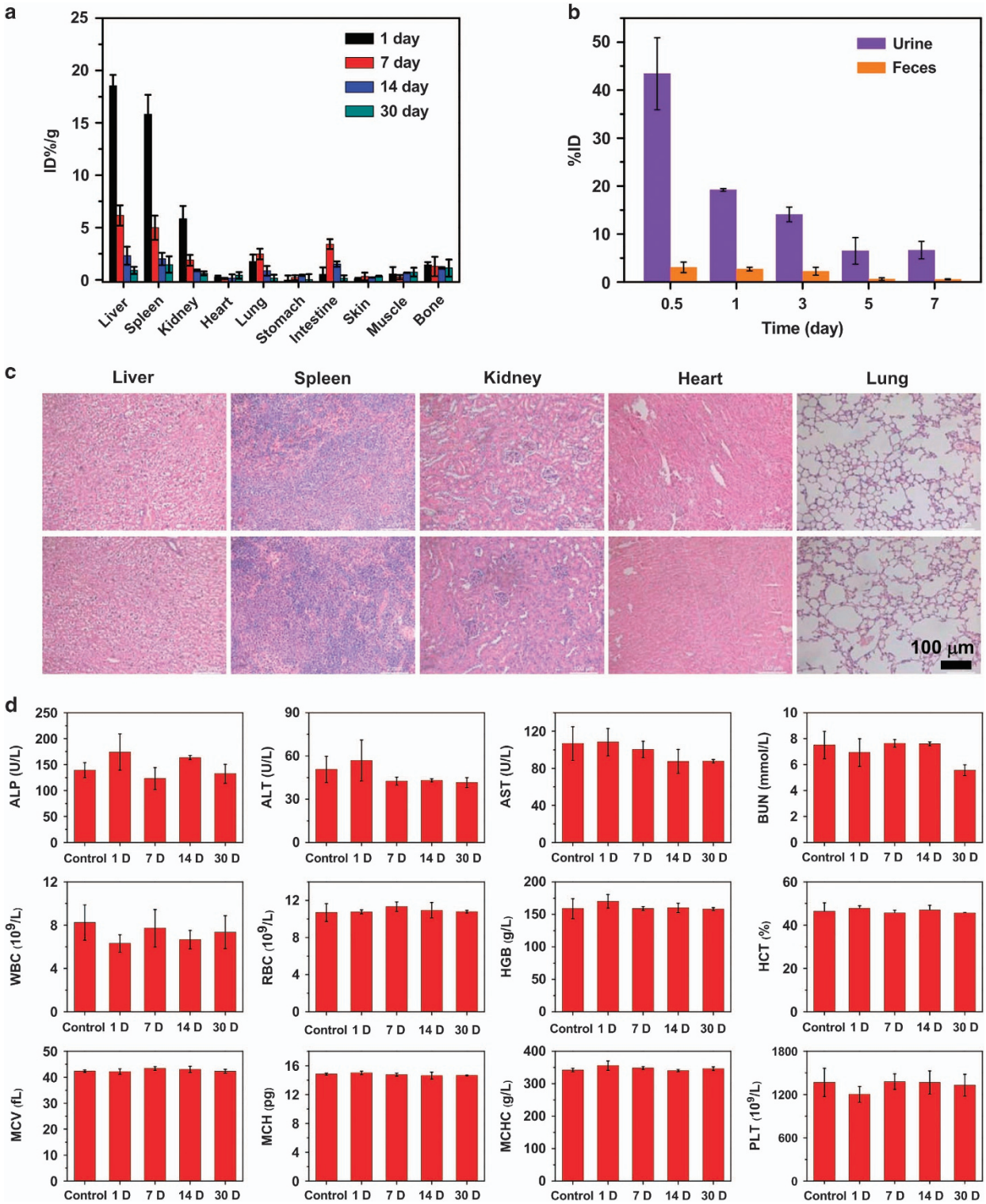

Figure 7 Biodistribution, clearance and *in vivo* long-term toxicity of NMOP-PEG. (**a**) Time-dependent biodistribution of Hf in mice after i.v. injection of NMOP-PEG. (**b**) Excretion profiles of Hf from NMOP-PEG injected mice at various times points after injection. (**c**) H&E-stained images of major organs from healthy control mice and mice after PPT and RT treatment. (**d**) Blood biochemistry and hematology data of female Balb/c mice treated with NMOP-PEG at a dose of 20 mg kg^{-1} at 1 day, 7 days, 14 days and 30 days p.i. The examined parameters included alkaline phosphatase (ALP), aminotransferase (ALT), aminotransferase (AST), blood urea nitrogen (BUN), white blood cell (WBC) counts, red blood cell (RBC) counts, hemoglobin (HGB), hematocrit (HCT), mean corpuscular volume (MCV), mean corpuscular hemoglobin (MCH), mean corpuscular hemoglobin concentration (MCHC) and platelets (PLT). All these parameters were close to those of the control healthy mice and within the normal reference ranges.

associated radio-resistance, leading to the excellent synergistic therapeutic effect of combined PTT and RT.

Composed of metal ions and organic ligands via non-covalent binding, metal-organic frameworks and metal-organic particles exhibit intrinsic biodegradability and may be cleared out from the body after degradation within the complicated *in vivo* environment.[27,37] We therefore carefully studied the long-term biodistribution and excretion behaviors of our NMOP-PEG. Balb/c mice were scarified at 1, 7, 15 and 30 days post intravenous injection of NMOP-PEG (20 mg kg^{-1}), and the major organs, including the liver, spleen, kidney, heart, hung, stomach, intestine, skin, muscle and bone, were collected, weighed and digested by aqua regia for a biodistribution study that was based on the detection of Hf levels in organs by ICP-AES (Figure 7a). The Hf levels were measured as ~18.5% ID g^{-1}, ~15.8% ID g^{-1} and ~5.8% ID g^{-1} in the liver, spleen and kidney, respectively, at 1 day post injection. After 30 days, however, the detected Hf levels decreased to ~2.3, ~2.0 and ~0.9% (%ID g^{-1}) in the liver, spleen and kidney, respectively, indicating that most of the injected NMOP-PEG had cleared out from the body. Furthermore, the Hf^{4+} concentrations in the feces and urine collected from mice injected with NMOP-PEG at different time intervals post injection were analyzed using ICP-AES to explore their possible clearance pathway. As shown in Figure 7b, we found that 43.4% and 7.52% of the injected Hf was cleared out of the body via urine and feces, respectively, within the first 12 h post injection High levels of Hf had been continuously detected in the mouse urine later on, suggesting that renal excretion could be the primary excretion pathway of the NMOP, although fecal excretion did occur simultaneously. Taken together, our results indicate that the Mn/Hf-IR825 NMOPs constructed from weak non-covalent bonds may be gradually dissociated into small ions and organic molecules once inside the complicated *in vivo* environment and may be able to undergo rapid renal filtration.[27,55]

Last, we looked into the potential toxic side-effects of the NMOP-PEG. The body weights of the mice after the injection of NMOP-PEG and the PPT and RT treatments did not significantly decrease, indicating the absence of acute toxicity of these nanoparticles to the treated mice (Supplementary Figure S9). We then carefully performed a hematology assay and histological examination of healthy Blab/c mice intravenous injected with NMOP-PEG (20 mg kg^{-1}). For the hematology assay, the blood samples were collected from mice at 1, 7, 15 and 30 days post intravenous injection of NMOP-PEG for serum, biochemical and blood panel analysis. During the whole treatment, all parameters remained constant in the control, untreated, healthy mice and within the normal reference ranges (Figure 7d). For the histological examination, samples of the liver, spleen, kidney, heart and lung were harvested and sliced for H&E staining (Figure 7c). No significant signs of abnormality induced by NMOP-PEG were observed in those organs within 30 days. Considering the almost complete excretion of NMOP-PEG from the body within a month, we conclude that NMOP-PEG nanoparticles are a relatively safe agent and will not lead to further long-term toxicity in treated mice at our tested dose.

CONCLUSION

In summary, core-shell and co-doped Mn/Hf-IR825 NMOPs were successfully prepared via a one-pot post-synthesis cation exchange method. With high r1 relaxivity and strong NIR and X-ray absorption, such NMOPs show excellent MR&CT&PA imaging contrast, and in the meantime, can be utilized for synergistic PTT&RT treatment of tumors with great therapeutic efficacy. This is attributed to the combined effects of the Hf-induced radio-sensitization and the PTT-induced tumor oxygenation that relieve tumor hypoxia-related RT resistance. Importantly, the nearly complete excretion of the Mn/Hf-IR825 NMOPs within 1 month and the absence of long-term toxicity to the treated mice encourage further *in vivo* applications as well as future clinical translations of NMOP-based nanoagents. To our best knowledge, this work is the first demonstration of using NMOPs for enhanced RT and synergistic thermo-radiotherapy by taking full advantage of both metal ions and organic ligands in a carrier-free NMOP system. Moreover, the facile post-synthesis cation exchange method to synthesize multi-component NMOPs developed in this work may be extended to the design and fabrication of other metal-organic particles- or metal-organic framework-related nanostructures with highly integrated functions, which is promising for biomedicine and other fields.

CONFLICT OF INTEREST

The authors declare no conflict of interest.

ACKNOWLEDGEMENTS

This work was partially supported by the National Basic Research Programs of China (973 Program) (2012CB932600), the National Natural Science Foundation of China (51525203, 51132006, 81403120), the Juangsu Natural Science Fund for Distinguished Young Scholars (BK20130005), the Collaborative Innovation Center of Suzhou Nano Science and Technology, a project funded by the Priority Academic Program Development (PAPD) of Jiangsu Higher Education Institutions, the Macao Science and Technology Development Fund (062/2013/A2) and the Research Fund of the University of Macau (MYRG2014-00033-ICMS-QRCM, MYRG2014-00051-ICMS-QRCM).

1 Jones, E. L., Prosnitz, L. R., Dewhirst, M. W., Marcom, P. K., Hardenbergh, P. H., Marks, L. B., Brizel, D. M. & Vujaskovic, Z. Thermochemoradiotherapy improves oxygenation in locally advanced breast cancer. *Clin. Cancer Res.* **10**, 4287–4293 (2004).
2 Dewar, J. A., Arriagada, R., Benhamou, S., Benhamou, E., Bretel, J. J., Pellae-Cosset, B., Marin, J. L., Petit, J. Y., Contesso, G. & Sarrazin, D. Local relapse and contralateral tumor rates in patients with breast cancer treated with conservative surgery and radiotherapy (Institut Gustave Roussy 1970–1982). *Cancer* **76**, 2260–2265 (1995).
3 Lord, C. J. & Ashworth, A. The DNA damage response and cancer therapy. *Nature* **481**, 287–294 (2012).
4 Wilson, W. R. & Hay, M. P. Targeting hypoxia in cancer therapy. *Nat. Rev. Cancer* **11**, 393–410 (2011).
5 Sun, X., Li, X.-F., Russell, J., Xing, L., Urano, M., Li, G. C., Humm, J. L. & Ling, C. C. Changes in tumor hypoxia induced by mild temperature hyperthermia as assessed by dual-tracer immunohistochemistry. *Radiother. Oncol.* **88**, 269–276 (2008).
6 Huang, W.-C., Chiang, W.-H., Cheng, Y.-H., Lin, W.-C., Yu, C.-F., Yen, C.-Y., Yeh, C.-K., Chern, C.-S., Chiang, C.-S. & Chiu, H.-C. Tumortropic monocyte-mediated delivery of echogenic polymer bubbles and therapeutic vesicles for chemotherapy of tumor hypoxia. *Biomaterials* **71**, 71–83 (2015).
7 Hu, J. L., Liu, L. P., Yang, S. L., Fang, X., Wen, L., Ren, Q. G. & Yu, C. Hepatitis B virus induces hypoxia-inducible factor-2α expression through hepatitis B virus X protein. *Oncol. Rep.* **35**, 1443–1448 (2016).
8 Cheng, L., Shen, S., Shi, S., Yi, Y., Wang, X., Song, G., Yang, K., Liu, G., Barnhart, T. E. & Cai, W. $FeSe_2$-decorated Bi_2Se_3 nanosheets fabricated via cation exchange for chelator-free 64Cu-labeling and multimodal image-guided photothermal-radiation therapy. *Adv. Funct. Mater.* **26**, 2185–2197 (2016).
9 Joh, D. Y., Sun, L., Stangl, M., Al Zaki, A., Murty, S., Santoiemma, P. P., Davis, J. J., Baumann, B. C., Alonso-Basanta, M. & Bhang, D. Selective targeting of brain tumors with gold nanoparticle-induced radiosensitization. *PLoS ONE* **8**, e62425 (2013).
10 Zhang, X. D., Luo, Z., Chen, J., Shen, X., Song, S., Sun, Y., Fan, S., Fan, F., Leong, D. T. & Xie, J. Ultrasmall Au10–12 (SG) 10–12 nanomolecules for high tumor specificity and cancer radiotherapy. *Adv. Mater.* **26**, 4565–4568 (2014).
11 Xiao, Q., Zheng, X., Bu, W., Ge, W., Zhang, S., Chen, F., Xing, H., Ren, Q., Fan, W. & Zhao, K. A core/satellite multifunctional nanotheranostic for *in vivo* imaging and tumor eradication by radiation/photothermal synergistic therapy. *J. Am. Chem. Soc.* **135**, 13041–13048 (2013).
12 Gai, S., Li, C., Yang, P. & Lin, J. Recent progress in rare earth micro/nanocrystals: soft chemical synthesis, luminescent properties, and biomedical applications. *Chem. Rev.* **114**, 2343–2389 (2013).

13 Zhang, C., Zhao, K., Bu, W., Ni, D., Liu, Y., Feng, J. & Shi, J. Marriage of scintillator and semiconductor for synchronous radiotherapy and deep photodynamic therapy with diminished oxygen dependence. *Angew. Chem. Int. Ed.* **127**, 1790–1794 (2015).
14 Yong, Y., Cheng, X., Bao, T., Zu, M., Yan, L., Yin, W., Ge, C., Wang, D., Gu, Z. & Zhao, Y. Tungsten sulfide quantum dots as multifunctional nanotheranostics for in vivo dual-modal image-guided photothermal/radiotherapy synergistic therapy. *ACS Nano* **9**, 12451–12463 (2015).
15 Yong, Y., Cheng, X., Bao, T., Zu, M., Yan, L., Yin, W., Ge, C., Wang, D., Gu, Z. & Zhao, Y. Tungsten sulfide quantum dots as multifunctional nanotheranostics for in vivo dual-modal image-guided photothermal/radiotherapy synergistic therapy. *ACS Nano* **9**, 12451–12463 (2015).
16 Li, H., Eddaoudi, M., O'Keeffe, M. & Yaghi, O. M. Design and synthesis of an exceptionally stable and highly porous metal-organic framework. *Nature* **402**, 276–279 (1999).
17 Lee, J., Farha, O. K., Roberts, J., Scheidt, K. A., Nguyen, S. T. & Hupp, J. T. Metal–organic framework materials as catalysts. *Chem. Soc. Rev.* **38**, 1450–1459 (2009).
18 Chen, B., Eddaoudi, M., Hyde, S., O'keeffe, M. & Yaghi, O. Interwoven metal-organic framework on a periodic minimal surface with extra-large pores. *Science* **291**, 1021–1023 (2001).
19 Chen, B., Ockwig, N. W., Millward, A. R., Contreras, D. S. & Yaghi, O. M. High H2 adsorption in a microporous metal–organic framework with open metal sites. *Angew. Chem. Int. Ed.* **117**, 4823–4827 (2005).
20 Kreno, L. E., Leong, K., Farha, O. K., Allendorf, M., Van Duyne, R. P. & Hupp, J. T. Metal–organic framework materials as chemical sensors. *Chem. Rev.* **112**, 1105–1125 (2011).
21 Dinca, M., Dailly, A., Liu, Y., Brown, C. M., Neumann, D. A. & Long, J. R. Hydrogen storage in a microporous metal-organic framework with exposed Mn^{2+} coordination sites. *J. Am. Chem. Soc.* **128**, 16876–16883 (2006).
22 Liu, B., Shioyama, H., Akita, T. & Xu, Q. Metal-organic framework as a template for porous carbon synthesis. *J. Am. Chem. Soc.* **130**, 5390–5391 (2008).
23 Li, P.-Z., Wang, X.-J., Liu, J., Lim, J. S., Zou, R. & Zhao, Y. A triazole-containing metal–organic framework as a highly effective and substrate size-dependent catalyst for CO_2 conversion. *J. Am. Chem. Soc.* **138**, 2142–2145 (2016).
24 Lv, Y., Shi, P., Shen, W., Chen, X. & Zhao, G. A series of novel Zn (II) and Mn (II) metal-organic frameworks constructed by 2,4-bis-oxyacetate-benzoic acid: syntheses, structures and photoluminescence. *Sci. China. Chem* **58**, 448–456 (2015).
25 Zhou, H., Li, M., Li, D., Zhang, J. & Chen, X. Thermal expansion behaviors of Mn (II)-pyridylbenzoate frameworks based on metal-carboxylate chains. *Sci. China Chem* **57**, 365–370 (2014).
26 Cai, W., Chu, C. C., Liu, G. & Wáng, Y. X. J. Metal–organic framework-based nanomedicine platforms for drug delivery and molecular imaging. *Small* **11**, 4806–4822 (2015).
27 Liu, D., Poon, C., Lu, K., He, C. & Lin, W. Self-assembled nanoscale coordination polymers with trigger release properties for effective anticancer therapy. *Nat. Commun.* **5**, 4182 (2014).
28 Horcajada, P., Chalati, T., Serre, C., Gillet, B., Sebrie, C., Baati, T., Eubank, J. F., Heurtaux, D., Clayette, P. & Kreuz, C. Porous metal-organic-framework nanoscale carriers as a potential platform for drug delivery and imaging. *Nat. Mater.* **9**, 172–178 (2010).
29 Della Rocca, J., Liu, D. & Lin, W. Nanoscale metal–organic frameworks for biomedical imaging and drug delivery. *Acc. Chem. Res.* **44**, 957–968 (2011).
30 An, J., Geib, S. J. & Rosi, N. L. Cation-triggered drug release from a porous zinc–adeninate metal–organic framework. *J. Am. Chem. Soc.* **131**, 8376–8377 (2009).
31 Keskin, S. & Kızılel, S. Biomedical applications of metal organic frameworks. *Ind. Eng. Chem. Res.* **50**, 1799–1812 (2011).
32 Zhou, H.-C., Long, J. R. & Yaghi, O. M. Introduction to metal–organic frameworks. *Chem. Rev.* **112**, 673–674 (2012).
33 Horcajada, P., Gref, R., Baati, T., Allan, P. K., Maurin, G., Couvreur, P., Férey, G., Morris, R. E. & Serre, C. Metal–organic frameworks in biomedicine. *Chem. Rev.* **112**, 1232–1268 (2011).
34 Feng, D., Gu, Z. Y., Li, J. R., Jiang, H. L., Wei, Z. & Zhou, H. C. Zirconium-metalloporphyrin PCN-222: mesoporous metal–organic frameworks with ultrahigh stability as biomimetic catalysts. *Angew. Chem. Int. Ed.* **124**, 10453–10456 (2012).
35 Park, J., Jiang, Q., Feng, D., Mao, L. & Zhou, H.-C. Size-controlled synthesis of porphyrinic metal–organic framework and functionalization for targeted photodynamic therapy. *J. Am. Chem. Soc.* **138**, 3518–3525 (2016).
36 Diring, S., Wang, D. O., Kim, C., Kondo, M., Chen, Y., Kitagawa, S., Kamei, K.-i. & Furukawa, S. Localized cell stimulation by nitric oxide using a photoactive porous coordination polymer platform. *Nat. Commun.* **4**, 2684 (2013).
37 Yang, Y., Liu, J., Liang, C., Feng, L., Fu, T., Dong, Z., Chao, Y., Li, Y., Lu, G. & Chen, M. Nanoscale metal-organic particles with rapid clearance for MR imaging guided photothermal therapy. *ACS Nano* **10**, 2774–2781 (2016).
38 Cheng, L., He, W., Gong, H., Wang, C., Chen, Q., Cheng, Z. & Liu, Z. PEGylated micelle nanoparticles encapsulating a non-fluorescent near-infrared organic dye as a safe and highly-effective photothermal agent for in vivo cancer therapy. *Adv. Funct. Mater.* **23**, 5893–5902 (2013).
39 Viswanathan, S., Kovacs, Z., Green, K. N., Ratnakar, S. J. & Sherry, A. D. Alternatives to gadolinium-based metal chelates for magnetic resonance imaging†. *Chem. Rev.* **110**, 2960–3018 (2010).
40 Taylor, K. M., Rieter, W. J. & Lin, W. Manganese-based nanoscale metal–organic frameworks for magnetic resonance imaging. *J. Am. Chem. Soc.* **130**, 14358–14359 (2008).
41 Ren, W., Tian, G., Zhou, L., Yin, W., Yan, L., Jin, S., Zu, Y., Li, S., Gu, Z. & Zhao, Y. Lanthanide ion-doped GdPO 4 nanorods with dual-modal bio-optical and magnetic resonance imaging properties. *Nanoscale* **4**, 3754–3760 (2012).
42 Mehravi, B., Ahmadi, M., Amanlou, M., Mostaar, A., Ardestani, M. S. & Ghalandarlaki, N. Conjugation of glucosamine with Gd^{3+}-based nanoporous silica using a heterobifunctional ANB-NOS crosslinker for imaging of cancer cells. *Int. J. Nanomed.* **8**, 3383–3394 (2013).
43 Boyle, W. S., Burk, L. M., Zhou, O. Z. & Lin, W. Zr-and Hf-based nanoscale metal–organic frameworks as contrast agents for computed tomography. *J. Mater. Chem.* **22**, 18139–18144 (2012).
44 Xia, A., Chen, M., Gao, Y., Wu, D., Feng, W. & Li, F. Gd^{3+} complex-modified NaLuF 4-based upconversion nanophosphors for trimodality imaging of NIR-to-NIR upconversion luminescence, X-Ray computed tomography and magnetic resonance. *Biomaterials* **33**, 5394–5405 (2012).
45 McCrary, J., Plassmann, E. H., Puckett, J., Conner, A. & Zimmermann, G. X-ray attenuation-coefficient measurements. *Phy. Rev.* **153**, 307 (1967).
46 Sidhu, S. & McGuire, J. An X-ray diffraction study of the hafnium-hydrogen system. *J. Appl. Phys.* **23**, 1257–1261 (1952).
47 Su, X.-Y., Liu, P.-D., Wu, H. & Gu, N. Enhancement of radiosensitization by metal-based nanoparticles in cancer radiation therapy. *Cancer Biol. Med.* **11**, 86–91 (2014).
48 Xu, M. & Wang, L. V. Photoacoustic imaging in biomedicine. *Rev. Sci. Instrum.* **77**, 041101 (2006).
49 Cheng, L., Liu, J., Gu, X., Gong, H., Shi, X., Liu, T., Wang, C., Wang, X., Liu, G. & Xing, H. PEGylated WS2 nanosheets as a multifunctional theranostic agent for in vivo dual-modal CT/photoacoustic imaging guided photothermal therapy. *Adv. Mater.* **26**, 1886–1893 (2014).
50 Zeng, J., Cheng, M., Wang, Y., Wen, L., Chen, L., Li, Z., Wu, Y., Gao, M. & Chai, Z. pH-responsive Fe(III)–gallic acid nanoparticles for in vivo photoacoustic imaging-guided photothermal therapy. *Adv. Health. Mater.* **5**, 772–780 (2016).
51 Sreejith, S., Joseph, J., Lin, M., Menon, N. V., Borah, P., Ng, H. J., Loong, Y. X., Kang, Y., Yu, S. W.-K. & Zhao, Y. Near-infrared squaraine dye encapsulated micelles for in vivo fluorescence and photoacoustic bimodal imaging. *ACS Nano* **9**, 5695–5704 (2015).
52 Song, K., Huang, P., Yi, C., Ning, B., Hu, S., Nie, L., Chen, X. & Nie, Z. Photoacoustic and colorimetric visualization of latent fingerprints. *ACS Nano* **9**, 12344–12348 (2015).
53 Jin, C. S., Lovell, J. F., Chen, J. & Zheng, G. Ablation of hypoxic tumors with dose-equivalent photothermal, but not photodynamic, therapy using a nanostructured porphyrin assembly. *ACS Nano* **7**, 2541–2550 (2013).
54 Song, G., Liang, C., Gong, H., Li, M., Zheng, X., Cheng, L., Yang, K., Jiang, X. & Liu, Z. Core–Shell MnSe@ Bi_2Se_3 fabricated via a cation exchange method as novel nanotheranostics for multimodal imaging and synergistic thermoradiotherapy. *Adv. Mater.* **27**, 6110–6117 (2015).
55 Chen, Q., Wang, C., Zhan, Z., He, W., Cheng, Z., Li, Y. & Liu, Z. Near-infrared dye bound albumin with separated imaging and therapy wavelength channels for imaging-guided photothermal therapy. *Biomaterials* **35**, 8206–8214 (2014).

Supplementary Information accompanies the paper on the NPG Asia Materials website (http://www.nature.com/am)